CrystEngComm

PAPER

View Article Online
View Journal | View Issue

Cite this: *CrystEngComm*, 2025, **27**, 6213

Influence of thorium dioxide powder synthesis methods on conventional and spark plasma sintering†

Sorin-Octavian Vălu,* Walter Bonani, Jacobus Boshoven, Karin Popa* and Marco Cologna

We investigated the influence of the synthesis method on the properties of ThO_2 powders and on their sinterability in conventional and spark plasma sintering (SPS). The powders were obtained by precipitation of thorium oxalate or thorium hydroxide, and further processed by low-temperature calcination at 600 °C or hydrothermal conversion at 250 °C. All powders had nanocrystallites <10 nm and a high surface area, which allow the onset of sintering at reduced temperatures. However, the presence of larger voids and non-ideal particle packing hinder full densification in the final sintering step. The powder obtained by hydrothermal decomposition of thorium hydroxide shows the highest specific surface area among all (SSA > 100 $m^2\ g^{-1}$) and reaches a relative density of ~90% in conventional pressure-less sintering at 1100 °C.

Received 2nd May 2025,
Accepted 24th June 2025

DOI: 10.1039/d5ce00459d

rsc.li/crystengcomm

Introduction

Thorium dioxide (ThO_2) shows favourable properties (*e.g.*, high melting point, high thermal conductivity, and strong radiation shielding) that makes it valuable in high-tech applications, particularly in the fields of nuclear energy, catalysis, high-temperature applications (crucibles, coatings, and refractory materials), optical glasses (cameras and telescope lenses), aerospace industry (paints), radiation protection, catalysis, *etc.*[1]

The thorium-based nuclear fuel cycle is of significant interest in nuclear energy due to its potential as an alternative to uranium (and plutonium) in nuclear reactors.[2,3] Oxide fuels such as $(U,Th)O_2$ or $(Pu,Th)O_2$ for fuelling nuclear reactors (*e.g.* light- or heavy-water reactors, gas-cooled fast reactors, *etc.*) would be typically used in the form of dense pellets. They can be produced by starting from a powder, which is pressed at room temperature and then sintered at high temperature for several hours, in a process called conventional or pressure-less sintering. The high melting point of ThO_2 (T_m = 3378 ± 17 °C)[4] makes it an excellent candidate for high-temperature applications, but at the same time it also poses challenges for the processing of ThO_2 ceramics.[5,6] The temperatures for densification of ThO_2 powders in conventional sintering often exceed 1700 °C.[7] The SPS technique (which employs pressure and pulsed direct current to heat and compact powders, allowing for high heating rates and reduced sintering temperatures and times) is increasingly utilized in the nuclear materials field[8] and has been successfully applied to ThO_2 as well.[9,10]

High-energy ball-milling has been used to increase the sinterability of commercial ThO_2 powders.[11] An alternative and effective way to enhance the sintering of such materials is by using nanoparticles.[12] In a larger context, research into actinide chemistry at the nanoscale has become increasingly important due to its potential to enhance safety and efficiency by reducing the grain size in the production of nuclear fuels. Over the past decades, numerous bottom-up methods have been employed to generate nanocrystalline ThO_2 and solid solutions.[13] The properties, such as size, shape, degree of agglomeration, chemical purity, *etc.*, are determined by the synthesis methods used, among which chemical precipitation, sol–gel, molten salts, hydro- and solvothermal processes, combustion synthesis, microwave-assisted synthesis, sonochemical synthesis, and laser ablation in liquid are some.[14–35] The precipitation of thorium ions (Th^{4+}) using hydroxides or oxalic acid, followed by thermal decomposition, are efficient and reproducible methods to fabricate agglomerates or aggregates of thorium dioxide (ThO_2) nanoparticles. Hydrothermal treatment of the resulting hydroxide or thorium oxalate can create nanoparticles of various sizes and shapes within the agglomerates. These characteristics influence the sintering behaviour of the powders.

European Commission, Joint Research Centre (JRC), Karlsruhe, Germany.
E-mail: octavian.valu@ec.europa.eu, karin.popa@ec.europa.eu

† Electronic supplementary information (ESI) available. See DOI: https://doi.org/10.1039/d5ce00459d

The goal of this study is to examine how the preparation method influences the properties of nanocrystalline ThO_2 powders during both conventional and spark plasma sintering.

Experimental

Powder preparation

All preparations were done in gloveboxes under an air atmosphere, while the thermal treatments were performed in a glovebox operating under nitrogen.

A stock Th-solution was prepared by dissolution of $Th(NO_3)_4{\cdot}5H_2O$ (Merck) in Milli-Q® water and acidified with nitric acid 65% (pH < 1). The concentration of this solution (as measured by ICP-MS) was 456 g Th l^{-1}.

Hydroxide route

A volume of 8 ml of this Th^{4+}–nitrate solution was added dropwise to 100 ml of 6 M ammonium hydroxide (Merck Millipore) at room temperature under stirring. The formed precipitate was left in the original solution (pH 12) overnight. 6.0 g of Th-hydroxide was separated after being filtered, washed with Milli-Q® water and dried over the weekend.

Half of the precipitate (3.0 g) underwent a 6 hour treatment at 600 °C under an air flow (1 l min^{-1}) with heating and cooling rates of 100 and 200 °C h^{-1}, respectively. For this purpose, a Linn Elektronik tubular (quartz) furnace and quartz crucible were used to obtain approximately 1.9 g of ThO_2 after the thermal treatment. This powder is hereinafter referred to as **HT** (hydroxide–thermal).

Another 2.9 g Th-hydroxide was mixed with 20 ml of Milli-Q® water and placed in a 100 ml autoclave (Parr Instruments model 4793, *p–T* controlled) with a glass insert that provides a free volume of about 80 ml. The mixture was then exposed to heat treatment for 4 hours at 250 °C at an autogenic pressure of *circa* 40 bar, from an initial nitrogen atmosphere. After cooling, the pressure in the autoclave returned to atmospheric pressure. After separation from the solution and subsequent washing with water, ethanol and acetone, an amount of approximately 1.9 g of ThO_2 was obtained. We will refer to this powder as **HH**, which stands for hydroxide–hydrothermal.

Oxalate route

In a similar manner, a volume of 8 ml Th^{4+}–nitrate stock solution was added dropwise at room temperature under stirring into 100 ml of oxalic acid 0.7 M (the as-called "reverse strike" approach); the oxalic acid solution was obtained by dissolution of oxalic acid dihydrate (VWR Chemicals) in Milli-Q® water and has an initial pH of 3. The formed precipitate was left ageing in the original solution overnight (pH does not change significantly after precipitation). 9.4 g of $Th(C_2O_4)_2{\cdot}xH_2O$ (as proved by XRD) was separated after filtration, washed with Milli-Q® water and dried over the weekend.

An amount of 4.7 g of the oxalate was subjected to a 6 hour treatment at 600 °C under an air atmosphere (heating and cooling rates of 100 and 200 °C h^{-1}, respectively). This temperature was selected as the minimum temperature needed to complete the thermal decomposition process.[36] Approximately, 2.3 g of ThO_2 was recovered after this heat treatment. This powder will be referred to as **OT** (oxalate – thermal) from this point forward.

Another portion of Th-oxalate weighing 4.5 g was added to 20 ml of Milli-Q® water, and the resulting mixture was placed in the 100 ml Parr autoclave with a glass insert, as described above. The system was then subjected to heat treatment at 250 °C and approximately 55 bar pressure for 4 hours under an initial nitrogen atmosphere (a peak temperature of 260 °C was initially applied for about 10 minutes in order to initiate the reaction). After cooling, the pressure in the autoclave was measured to be around 15 bar at room temperature, indicating that the decomposition reaction had been completed. Note that the atmosphere in the autoclave changes from an inert atmosphere to a reducing atmosphere due to the formation of CO (and CO_2) as a reaction product of the oxalate decomposition. However, the oxidation state of the thorium remains unaffected during the conversion from oxalate to oxide. After separation from the solution, it was washed with water, ethanol and acetone, and approximately 3.0 g of ThO_2 was obtained. In the following, this powder will be referred to as **OH** (oxalate – hydrothermal).

For conventional or spark plasma sintering, all powders were used as-prepared, with no milling or grinding.

Pellet preparation

Pressing and conventional sintering. Amounts of 100–160 mg of powder were compacted using a bi-directional press (Lauffer VIUG16) in a 5 mm diameter die with a load of 7.9 kN (~400 MPa). The powder did not contain any additives. The die cavity was only lubricated by pressing pellets made of pure zinc-stearate, to form a film on the surface of the tungsten carbide die and to reduce the friction between the ceramic pellets and the die.

The disks were placed in a molybdenum container and sintered under reductive gas in a cold wall sinter furnace (Degussa VSL10/18). The temperature of the furnace was measured with a type C thermocouple, placed close to the samples. Two different kinds of experiments were conducted, referred to as step sintering and direct sintering.

Step sintering: one disc of each powder (the only exception is **OT** powder, where three discs were used) was heat treated for four hours at 1100, 1300, 1500, 1600, and 1700 °C with a heating rate of 200 °C h^{-1}. After cooling at room temperature, the dimensions of the pellets were taken after each heat treatment and the samples were placed back into the furnace for the next thermal treatment.

Direct sintering: one disc of each powder was sintered for four hours directly at 1600 °C, with the same heating rate.

The geometrical densities of all pellets were calculated by measuring the weight (Mettler-Toledo AG204), the diameter and the height (Mitutoyo QuickMike). The dimensions were

measured several times under different orientations. The resulting average values were determined and registered. The relative densities of the discs were calculated taking a crystallographic density of ThO_2 of 10.0 g cm^{-3} at room temperature.[37,38]

Spark plasma sintering. Spark plasma sintering was performed with a small-scale SPS (FCT, GmbH, Rauenstein, Germany) confined within a glovebox for handling radioactive powders.[39] Graphite dies of 6 mm diameter were filled with *ca.* 350 mg of powder and pre-compacted at 18 MPa before mounting them in the SPS. No separation foils were used between the powder and graphite dies. Sintering was performed in a vacuum, under a uniaxial pressure of 70 MPa applied from room temperature on, with a heating and cooling rate of 100 °C min^{-1}, at the maximum temperatures of either 1100 °C or 1600 °C and a dwell time of 10 min.

Characterisation methods

X-Ray Diffraction (XRD). The crystalline structure/purity of the products was determined at room temperature by powder XRD using a Bruker D8 X-ray diffractometer mounted in a Bragg–Brentano configuration with a curved Ge monochromator (1,1,1) and a copper tube (40 kV, 40 mA) equipped with a LynxEye position sensitive detector. Structural analyses were performed by profile matching. The average crystallite size was estimated from the XRD line broadening using the Scherrer equation.[40]

Morphological characterisation. Scanning electron microscopy (SEM) analysis was performed on the uncoated fractured surface of the samples using a Thermo Scientific Quattro Scanning Electron Microscope fitted with an energy-dispersive X-ray spectroscopy (EDS) XFlash 6/30 detector.

Evaluation of the specific surface area (SSA). The SSA was evaluated *via* the Brunauer–Emmett–Teller (BET) method[41] from N_2 physisorption isotherms at −196 °C collected with a surface area analyser (Gemini VII 2390 Series, Micromeritics) in the range 0.05–0.30 p/p_0. The degassing system, a sample chamber and a Dewar vessel are enclosed in an alpha-tight glovebox, for measurements of radioactive samples. The main body, with a pressure measurement system and embedded electronics is placed outside of the glovebox and connected through appropriate feedthroughs. Evaluation of data was done with MicroActive software provided by Micromeritics.

Spectroscopic characterisation. FTIR spectroscopy was performed on the pulverised sample material in attenuated total reflectance mode with an Alpha Platinum Bruker spectrometer equipped with a ZnSe crystal. The spectra were obtained in a wavenumber range from 600 to 4000 cm^{-1} with a resolution of 4 cm^{-1}.

Results and discussion

Thorium hydroxide and thorium oxalate precursors

The two precursors were characterised by XRD, SEM and FT-IR.

The XRD pattern (Fig. S1†) indicates that Th-hydroxide is almost amorphous, in agreement with the findings reported in ref. 42, and the baseline being very little deformed around the main diffraction lines of ThO_2. The two peaks at 3600 and 3100 cm^{-1} of the FT-IR spectrum indicate the presence of $ThO_2{\cdot}xH_2O$ as well (Fig. S2†). After hydrothermal treatment, $Th(OH)_4$ de-hydrated and/or reorganised in as $ThO_2{\cdot}xH_2O$ (x = 0–2), as proved by XRD. A similar behaviour was observed for ceric hydroxide.[43] The micrographs (Fig. 1) show very fine particles within larger aggregates of irregular shape. Some of these aggregates show a layer that looks dense at the highest SEM magnification, which could have formed during the filtration of the precipitate.

For the second precursor, the XRD indicates a well crystallised $Th(C_2O_4)_2{\cdot}xH_2O$ monoclinic ($C2/c$) compound. SEM provides very important information regarding the morphology of the powder: we have applied the "reverse strike" approach, meaning addition of a highly concentrated Th-solution (pH < 1) in a highly concentrated oxalic acid solution; the oxalate platelets (Fig. 1) are, however, cavitated, similar to those obtained by[36] using the "direct strike" method (addition of oxalic acid solution into a Th-solution).

The FT-IR spectrum (Fig. S2†) shows a typical pattern of the absorption peak of crystallised $Th(C_2O_4)_2{\cdot}xH_2O$.[31] Several non-resolved adsorption bands in the range 3000–3500 cm^{-1} can be attributed to the different stretching modes of the O–H bond of hydrate oxalate groups. The sharp adsorption peaks at 1630, 1350, 1310 and 795 cm^{-1} are assigned to the symmetric stretching of C═O, asymmetric and symmetric C–O stretching and O–C═O asymmetric stretching vibration modes, respectively.

ThO_2 powder characterisation

Table 1 summarises several physical properties of the powders obtained by different methods. The temperatures of the processes were selected as the minimum needed for the thermal[36] and hydrothermal[21,25] decomposition of the oxalate. As a matter of coincidence, the crystallite sizes are similar (~6.5 and ~8 nm for the two pairs of thermal and hydrothermal processes, respectively). The crystallite sizes produced from hydroxides are smaller than those obtained from oxalates.[43–45] The lattice parameters are larger than the one reported for bulk ThO_2 (0.5598 nm) and pairing as a function of the type of the method (thermal or hydrothermal), with larger values obtained for the hydrothermal processes, possibly due to adsorbed water (Fig. S3†).

The synthesis method has a significant effect on the SSA. While the thermal method gives the smallest values (17 and 13 m^2 g^{-1} for **HT** and **OT**, respectively), these values are far larger for the hydrothermal treatment (110 and 35 m^2 g^{-1} for **HH** and **OH**, respectively), in line with the milder conditions of the processes. An equivalent particle size, d_{BET}, was calculated from the SSA, assuming the ideal case of spherical and isolated primary particles, using the formula $d_{BET} = 6/(SSA{\cdot}\rho)$, with ρ = 10.0 g cm^{-3} (Table 1). The particle size

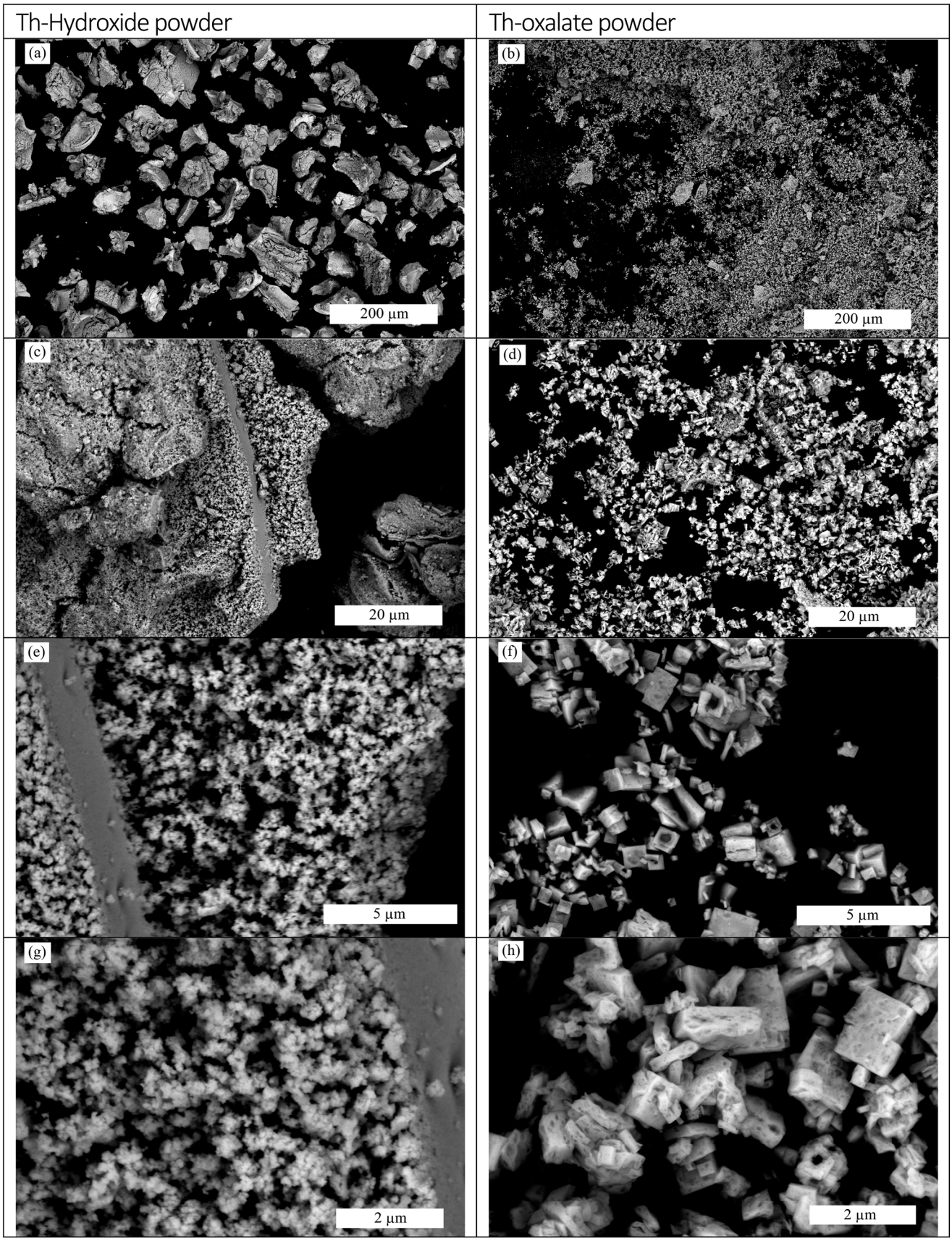

Fig. 1 SEM images of the Th-hydroxide ((a), (c), (e) and (g)) and Th-oxalate hydrate ((b), (d), (f) and (h)) powders.

Table 1 Experimental details on powder preparation and characterisation

Powder preparation method				
Reaction conditions	Hydroxide thermal **HT**	Hydroxide hydrothermal **HH**	Oxalate thermal **OT**	Oxalate hydrothermal **OH**
T, °C	600	250	600	250
p, bar	1	40	1	55
Atmosphere	Oxidising (air)	Inert (N_2)	Oxidising (air)	Inert (N_2) + CO/CO_2 formed *in situ*
ThO_2 powder characteristics				
a, nm	0.5605(2)	0.5615(1)	0.5605(1)	0.5614(2)
d from XRD, nm	6.6 ± 1.1	6.2 ± 0.8	7.8 ± 0.9	8.1 ± 1.2
SSA, $m^2\ g^{-1}$	17.3 ± 0.3	109.7 ± 0.3	12.9 ± 0.1	35.0 ± 0.7
Equivalent spherical particle size, d_{BET}, nm	34.7	5.5	46.5	17.1
Morphology from SEM	100–500 μm agglomerates of nanometric powders	100–500 μm agglomerates of nanometric powders	Cavitated plate-like aggregates of 0.5–1 μm	Core shell spherical agglomerates of ~0.3 μm

calculated from the SSA is generally higher than the crystallite size calculated by XRD, indicating that a part of the surface of the sample is inaccessible. This could be due to agglomeration/aggregation or partial sintering of the crystallites. Interestingly, only the SSA for the powder obtained by hydrothermal methods give a calculated particle size in fair agreement with the one obtained from XRD. In the case of **HH** powder, the close similarity in value suggests that the primary particles and crystallites are the same.

SEM (Fig. 2) and FTIR (Fig. S4†) techniques were used to elucidate this behaviour. All FTIR measurements indicate the presence of water and organic compounds, and the general features of the IR spectra are closer to the one of the precursors (Fig. S4†). The thermal method gives almost pure ThO_2 powders. Several features that might be assigned to carbon pollution are present in the powders obtained from oxalate, as the signals at 1510 cm^{-1} and 1360 cm^{-1} (ν_{as} C═O), and 1100 cm^{-1} (ν_s C═O).[46] The two vibrations present at 980 and 870 cm^{-1} in the powders obtained by hydrothermal treatments could not be assigned but are likely related to the presence of an impurity in the autoclave.

Both powders obtained from the hydroxide (**HT** and **HH**) show large agglomerates, which are pseudomorphic for the powder obtained by thermal decomposition (Fig. 2 and Fig. 1, respectively). Such agglomerates are composed of nanometric particles, as shown by XRD and BET (Table 1). The apparently dense layer observed in the precursor is still present in the HT powder. Thermal oxalate-to-oxide conversion (**OT**) is also pseudomorphic and results in agglomerates of nanocrystallites preserving the original size and shape of the oxalate. On the other hand, the hydrothermal treatment (**OH**) results in almost independent and fairly monodispersed cavitated spheroids, corresponding to agglomerated ThO_2 nanoparticles.

ThO_2 pellet sintering and characterisation

Spark plasma sintering. The SPS densification curves at a constant pressure of 70 MPa are given in Fig. 3 (max T 1100 °C) and Fig. 4 (max T 1600 °C). The graphs show the displacement of the upper piston and the temperature as a function of time. The piston displacement is a direct indication of the densification of the pellet and also includes the thermal expansion of the system. A positive displacement rate indicates that the piston moves downwards, for example, due to pellet densification or thermal contraction during cooling, while thermal expansion during heating gives a negative displacement rate. Since the thermal expansions of the system are close to linear (see for *e.g.* the cooling part of Fig. 3 and 4), one can easily extract information on the sintering behaviour from the piston displacement curve. The sintering behaviour of each powder is qualitatively reproducible (first part of Fig. 3 and 4, up to 1100 °C). All samples fractured in several pieces after SPS, so that it was not possible to determine the geometrical density. The density can be inferred from the SEM microstructures.

The two powders obtained by hydrothermal decomposition (**HH** and **OH**) show a very similar behaviour, with the **HH** curve slightly shifted to lower temperatures (~50 °C): (i) an initial low-temperature shrinkage up to ~400 °C, (ii) a steep sintering curve between ~800 °C and ~1300 °C, and (iii) the isothermal dwell, where densification continues at a much lower rate.

The first low-temperature shrinkage has been previously observed with nanometric powders and was attributed to degassing of the adsorbed species and particles and agglomerate rearrangement.[47] Most of the densification happens in the second step, up to ~1300 °C, due to the sintering of the primary nanometric particles and the elimination of the nanoporosity. The negative slope of the displacement above 1300 °C indicates that the thermal expansion of the system (sample and pistons) is larger than the sintering shrinkage. Since the slope is almost linear and opposite to the slope of the displacement during cooling, we can conclude that the sintering rate is negligible in comparison to the thermal expansion above 1300 °C. Finally, densification continues very slowly also during the isothermal dwell at 1600 °C. This last phase likely represents

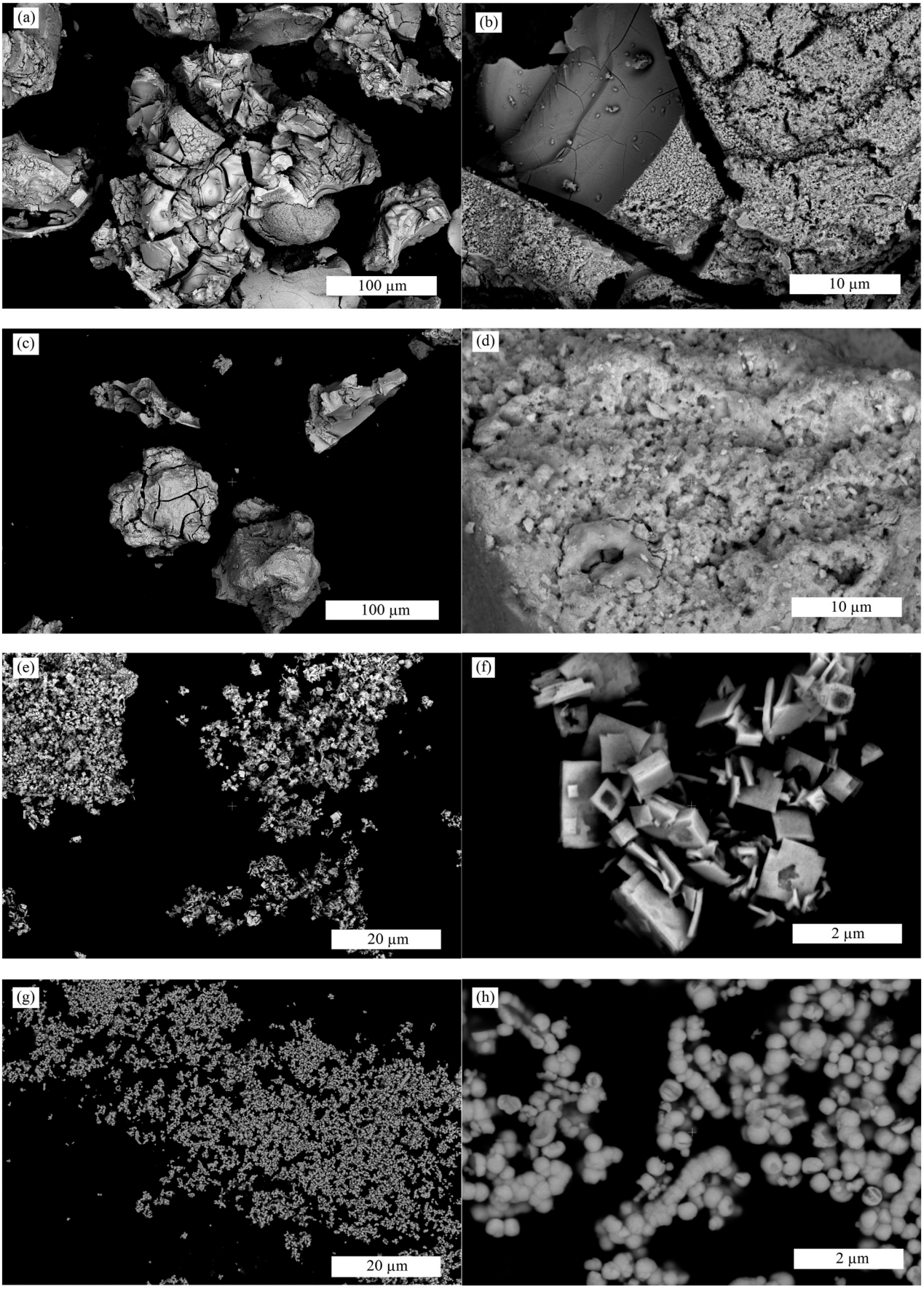

Fig. 2 SEM images of the ThO_2 powders obtained by different methods: **HT** (a) and (b); **HH** (c) and (d); **OT** (e) and (f); **OH** (g) and (h).

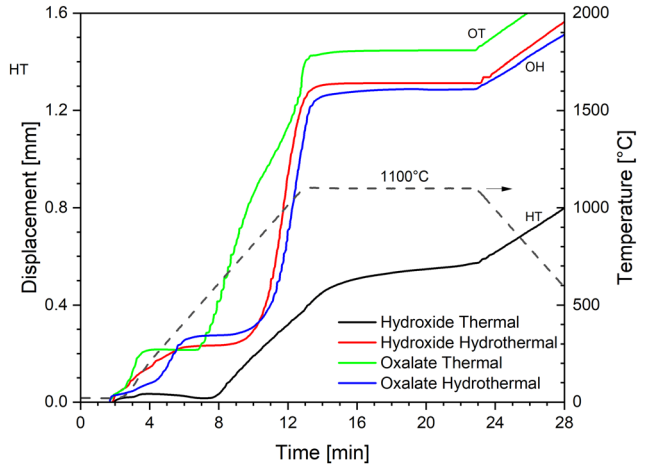

Fig. 3 SPS densification curves at a maximum temperature of 1100 °C with a constant pressure of 70 MPa.

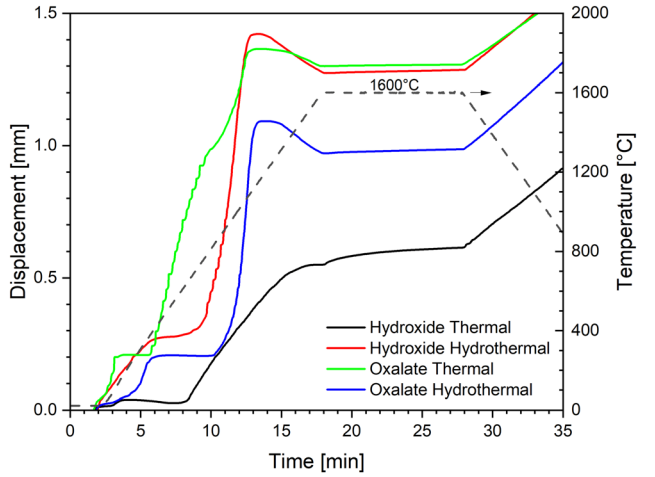

Fig. 4 SPS densification curves at a maximum temperature of 1600 °C with a constant pressure of 70 MPa.

the elimination of the larger porosity, which is present between the agglomerates. The similar sintering curves of the **HH** and **OH** powders suggest that the hydrothermal treatment gives similar products in terms of the morphological features influencing the densification rate (*e.g.* the degree of agglomeration, packing, shape and size of the primary particles), and thus the final oxides show little memory of their precursor's shape (oxalate or hydroxide).

This is not the case for the simply calcined powders: **HT** and **OT** show two completely distinct sintering curves. The **OT** powder shows an initial compaction below 200 °C, then the on-set of sintering at a very low temperature (~400 °C), after which the densification continues in at least two main steps (indicatively 400–1000 °C and 1000–1600 °C). Such behaviour is typical of powder compacts with small primary particle sizes organised in larger agglomerates, resulting in a microstructure with porosity at two distinct scales, nanometric and micrometric. In particular, it has been shown that ex-oxalate urania and thoria powders produced under similar conditions consist of nanometric primary particles, ordered within larger thin platelets of micrometric size. In this configuration, the nanoparticles influences the low-temperature sintering, while the shape and packing of the platelets dominate the densification kinetics at high temperature.[18,48]

Lastly, the hydroxide powder thermally calcined (**HT**) also shows an initial compaction below 200 °C (but much lower than that of all the other powders), then it starts sintering at ~600 °C, and the sintering range extends up to 1600 °C and continues during the dwell time. It can be inferred that the particle size and porosity distribution for this powder is relatively large, and the residual large porosity between the agglomerates are responsible for the high-temperature densification.

The fracture surfaces after sintering at 1100 °C (Fig. 5) and 1600 °C (Fig. 6) provide further insight into the process. At 1100 °C, the microstructure of **HT** presents an area of well-sintered grains (0.3–1.2 μm size) within the original agglomerates. These areas are surrounded by large voids, partially filled by zones with less-sintered powder (~50 nm size), which do appear to have been affected by the external force applied during SPS, as the pressure was likely concentrated on the skeleton made by the larger agglomerates. Raising the temperature to 1600 °C increases and homogenises the grain size and partially removes the large voids, possibly by creep and deformation of the large agglomerates. However, the time and temperature are not sufficient for completely removing the voids.

The **HH** powder at 1100 °C not only shows very fine grains (~100 nm) surrounded by distributed nano-porosity, but also few areas with larger micrometric-sized grains (not shown here). Some elongated flaws are still visible around the original powder agglomerates but are much less than in the **HT** sample. It appears that the hydrothermal decomposition is effective in destroying the original agglomerates and producing softer agglomerates that are easily deformed under pressure to fill the gaps during the SPS process. At 1600 °C the grains have grown to a few micrometers in size, but the intergranular porosity is not completely eliminated, and some grains have assumed a peculiar rounded shape that could be caused by the incomplete elimination of some impurity or trapped gas during sintering. This confirms previous results, which have shown that incomplete densification is obtained under similar conditions, but dense and nanostructured (50 nm grain size) pellets can be achieved with an **HH** powder by rising the pressure to 500 MPa in a special high-pressure SPS set-up using SiC dies, at temperatures of only 915 °C.[47]

The **OT** powder at 1100 °C gives a fine microstructure with grains of *ca.* 800 nm surrounded by residual closed porosity, and some regions with larger grains in the order of a few micrometres, located towards the centre of the pellet. At 1600 °C the porosity is almost completely eliminated, and the mean grain size has grown to 3.5 μm, in agreement with the findings in ref. 10 and 18, where relative

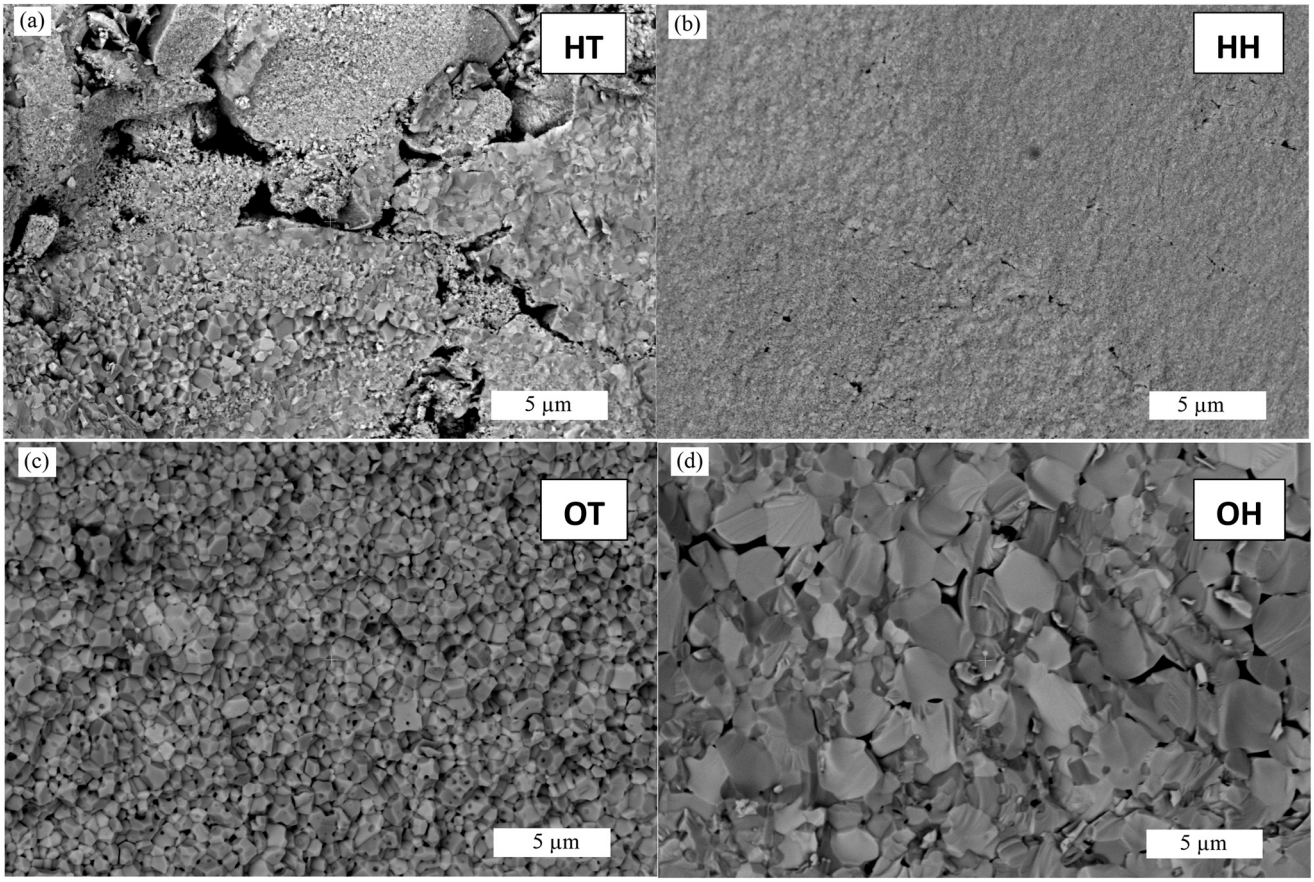

Fig. 5 SEM micrographs of selected fracture surfaces after SPS for 10 min at 1100 °C (scale bar 5 μm). **HT** (a); **HH** (b); **OT** (c); **OH** (d).

densities above 95% and comparable grain sizes under similar processing conditions and powders were obtained.

Lastly, the **OH** powder at 1100 °C has grown into larger grains of *ca.* 3 μm in size, some of them with a rounded shape. The microstructure after SPS at 1600 °C looks close to fully dense and the grain size approaches 10 μm. While **HH** and **OT** ThO_2 powders have been previously sintered in SPS, a comparison with the literature for **HT** and **OH** powder is not possible, as no previous results were found.

Conventional pressure-less sintering. Green samples were densified also by conventional pressure-less sintering as detailed in the experimental section. After a single heat treatment for 4 h at 1600 °C, the relative density for **HT**, **HH**, **OT** and **OH** were 69.1%, 79.7%, 90.6% and 79.5% and the mass losses 2.1%, 4.9%, 2.0% and 9.5%, respectively. The mass loss in ThO_2 is believed to be due to the release of the adsorbed species as CO/CO_2 and H_2O.[36] In the hydrothermally treated powders, the mass loss is much higher than that in the thermally treated ones. For such powders, most of the densification is achieved already at 1100 °C (step-sintering test curves in Fig. 7 and data in Table S1†), probably because of the nanometric size of the primary particles. However, the larger porosity and possibly the voids left by a large volume of the material that evaporates requires a much higher temperature to complete densification. The highest density and lowest mass loss are achieved with the ex-oxalate simply calcined powder (**OT**), which continues to densify up to 1700 °C. IR measurements performed on samples treated at 1600 °C (Fig. S6†) indicate that the powders are free of carbon contamination. The sample obtained by hydrothermal treatment of hydroxide is the only one in which the same impurities as those found in the parent sample can be identified.

The microstructures are shown in Fig. 8. The **HT** sample appears poorly sintered, in agreement with its low relative density, and the original agglomerates with the peculiar dense layer observed in the powders are clearly recognisable. Conversely, the particles of the **HH** sample have sintered and grown to grains of several micrometres in size, which show partially intragranular fracture. The residual porosity is well-distributed and intergranular, while larger elongated flaws between the original agglomerates (visible at lower magnifications, not shown here) also contribute to the overall low relative density. Interestingly, this sample achieves the highest density already at 1100 °C, after which the increasing temperature gives only grain growth but has little effect on the densification and elimination of the larger pores and flaws. The **OT** sample reaches the highest density, giving a homogeneous microstructure with distributed porosity

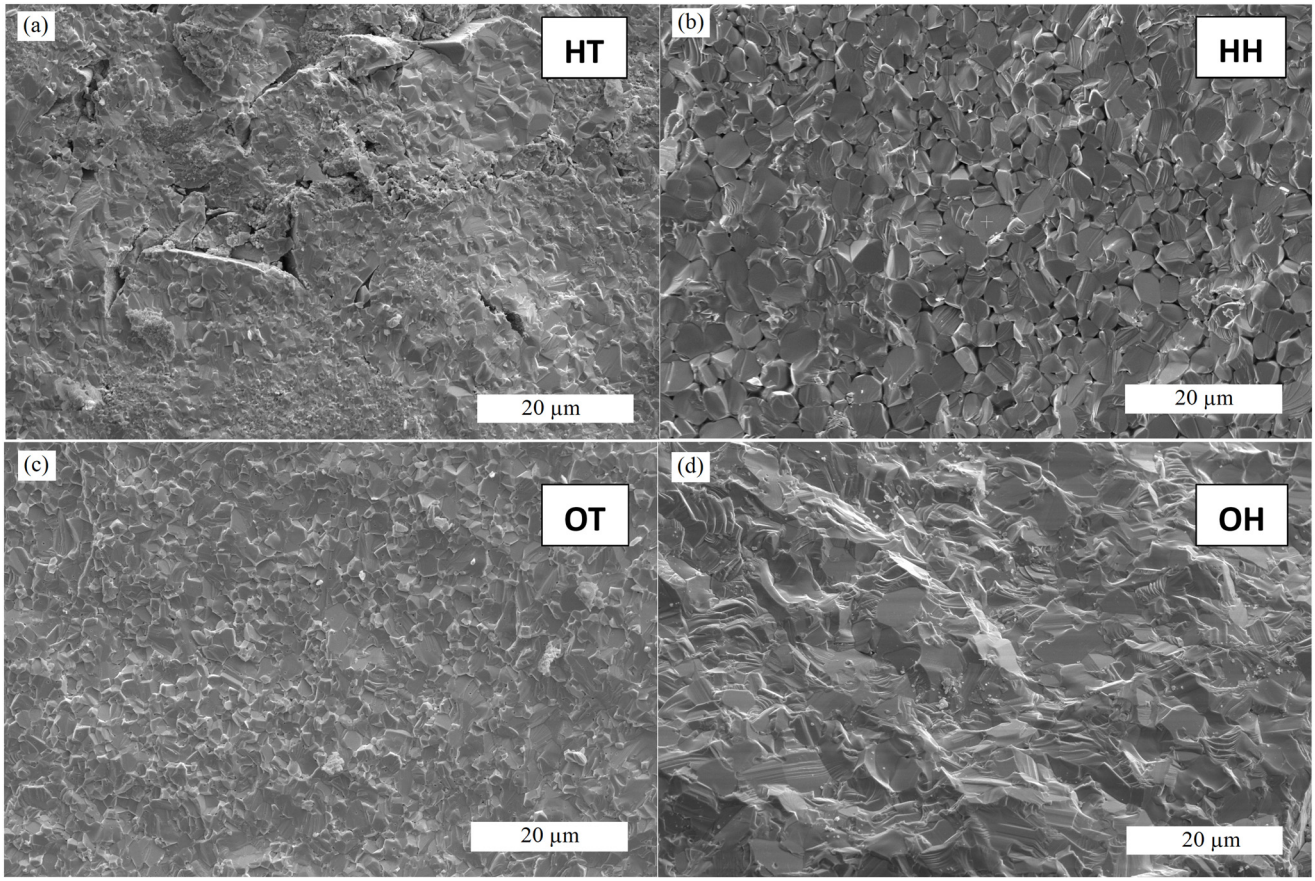

Fig. 6 SEM micrographs of selected fracture surfaces after SPS for 10 min at 1600 °C (scale bar 20 μm; note the lower magnification compared to Fig. 5). **HT** (a); **HH** (b); **OT** (c); **OH** (d).

between the original micrometric-sized platelets. The negative effects of larger powder aggregates are less severe than those in the **HT** and **HH** powders. The sintering behaviour of analogously produced powders have been extensively studied in the literature (*e.g.* ref. 36 and 49). It is typically seen that the densification happens in two main stages: initial removal of the small intra-platelet porosity at lower temperatures, followed by the elimination of the larger intra-platelet porosity at higher temperatures. Very high densities (>95%) can be achieved at higher temperatures (>1700 °C). Finally, the **OH** sample shows sintered grains of a few micrometres in size, surrounded by large micrometric pores. Analogous to the other hydrothermally-produced powder (**OH**), increasing the sintering temperature from 1100 °C to 1600 °C does not improve the final density, but instead promotes grain growth.

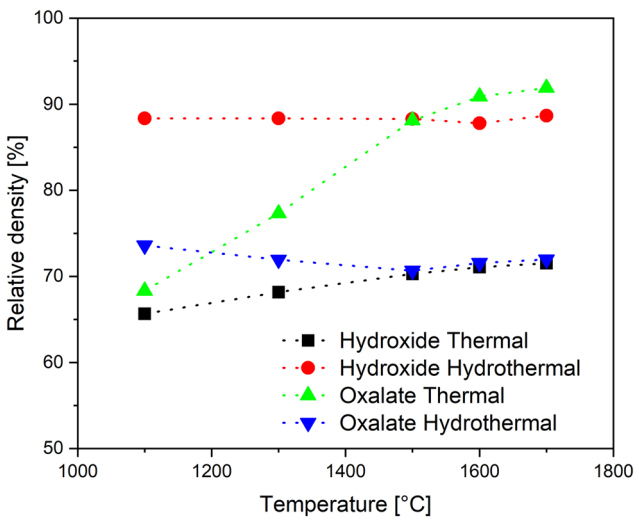

Fig. 7 Relative density during conventional sintering from 1100 °C to 1700 °C (step-sintering test).

Conclusions

We synthetized four different ThO_2 powders, starting from two different precursors (either thorium hydroxide or thorium oxalate), and applying two distinct conversion routes (either low-temperature calcination at 600 °C or hydrothermal conversion at 250 °C). Each method yields powders containing nanocrystallites (<10 nm) but with distinct properties, such as the degree of agglomeration/aggregation, specific surface area and residual water content. Hydrothermal decomposition produces powders with a higher specific surface area compared to those

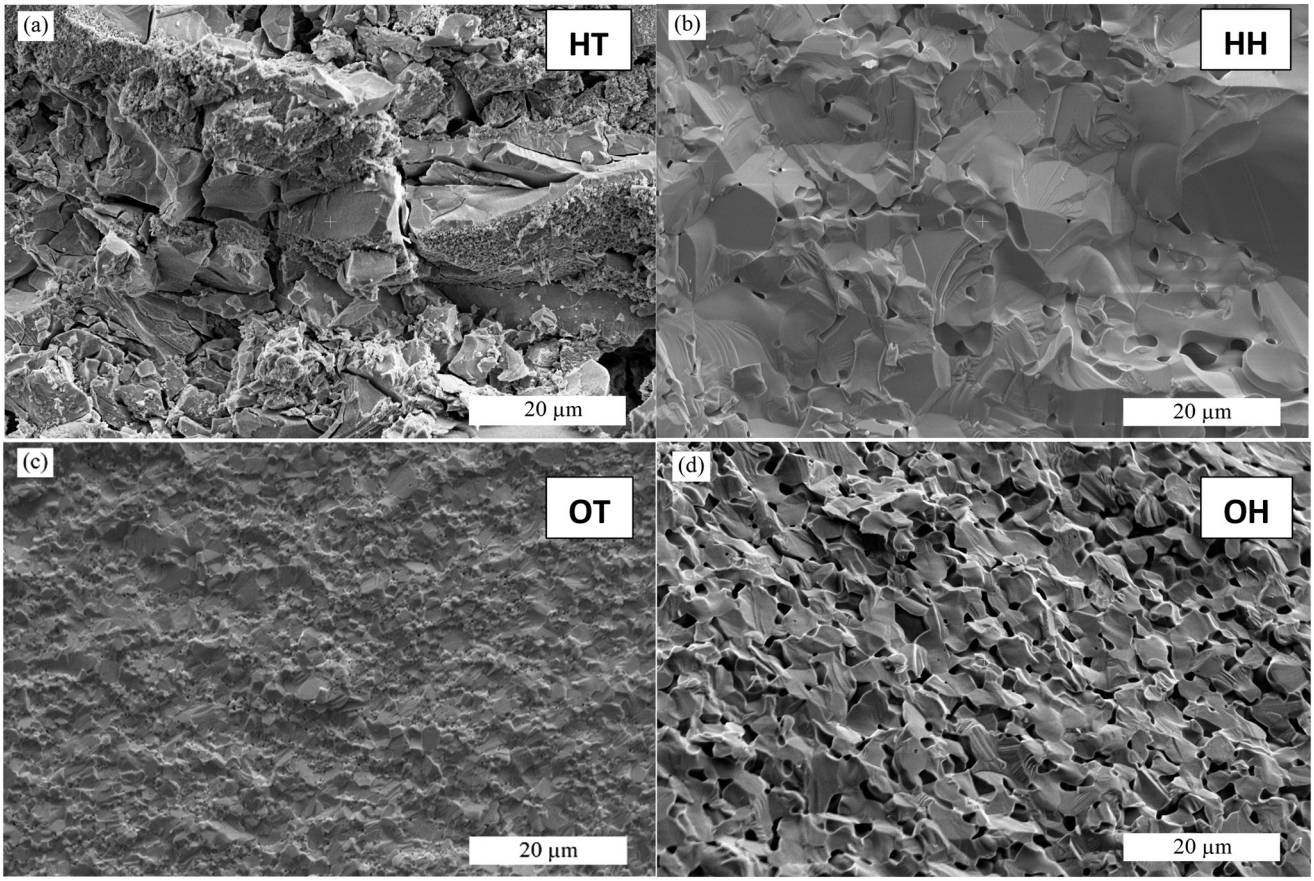

Fig. 8 SEM micrographs of the selected fracture surfaces after conventional sintering for 4 h at 1600 °C (same magnification as in Fig. 6). **HT** (a); **HH** (b); **OT** (c); **OH** (d).

obtained through thermal calcination. Among all the samples, the powder obtained from hydrothermal decomposition of Th hydroxide shows the highest specific surface area (SSA $>$ 100 m^2 g^{-1}). On the other hand, the powders obtained by hydrothermal decomposition contain more residual water and show the highest mass loss during sintering.

The properties of the powders dictate the sintering behaviour. The nanometric size of the primary particles induce an initial fast sintering at low temperatures in both SPS and conventional sintering. However, the presence of large voids left between the agglomerates/aggregates and the degassing of the adsorbed water hinders further densification at low temperatures unless external pressure is applied during sintering, as in SPS. In particular, the very large surface area powder obtained by hydrothermal decomposition of Th hydroxide shows the highest potential for low-temperature sintering: it reached a relative density of almost 90% already at temperatures as low as 1100 °C in conventional sintering. Any further increase in the temperature up to 1600 °C did not improve the density. Additional processing and optimisation steps, *e.g.* degassing, and better particle packing by de-agglomeration/de-aggregation and granulation could also improve the final densification step.

Data availability

The data that support the findings of this study are available from the authors upon reasonable request.

Author contributions

S.-O. V.: methodology, investigation, data curation, and writing – review and editing; W. B.: methodology, investigation, and writing – review and editing; J. B.: investigation and writing – review and editing; K. P.: conceptualization, methodology, investigation, writing – original draft, review and editing, and supervision; M. C.: conceptualization, methodology, validation, investigation, data curation, writing – original draft, review and editing, and supervision.

Conflicts of interest

There are no conflicts to declare.

Notes and references

1 X.-W. Wang, L. Mei, L.-Y. Yuan, S.-A. Wang, Z.-F. Chaiac and W.-Q. Shi, Size-tunable synthesis of monodisperse thorium dioxide nanoparticles and their performance on the

adsorption of dye molecules, *CrystEngComm*, 2014, **60**, 10469–10475.
2 U. Humphrey and M. Khandaker, Viability of thorium-based nuclear fuel cycle for the next generation nuclear reactor: Issues and prospects, *Renewable Sustainable Energy Rev.*, 2018, **97**, 259–275.
3 M. Du Toit, F. Van Niekerk and S. Amirkhosravi, Review of thorium-containing fuels in LWRs, *Prog. Nucl. Energy*, 2024, **170**, 105136.
4 C. Ronchi and J. Hiernaut, Experimental measurement of pre-melting and melting of thorium dioxide, *J. Alloys Compd.*, 1996, **240**(1–2), 179–185.
5 H. Takiishi, L. Gênova, E. Cavalheira, M. Cotrim, W. Santos and P. Lainetti, Use of dopants for thoria sintering temperature reduction-characterization of ThO2, *J. Energy Power Eng.*, 2016, **10**, 740–745.
6 O. Shichalin, R. Frolov, I. Buravlev, I. Tanayev, V. Faizova, S. Azon, N. Andreeva and E. Papynov, Synthesis and Spark Plasma Sintering of microcrystalline thorium dioxide for nuclear fuel products, *Russ. J. Inorg. Chem.*, 2020, **65**, 1245–1252.
7 S. Qi, F. Guan, D. Peng, X. Zhang and W. Liao, A simple method for preparing ThO2 ceramics with high density, *Int. J. Appl. Ceram. Technol.*, 2023, **20**(2), 1194–1204.
8 M. Cologna, 5.25 - Use of field assisted sintering for innovation in nuclear ceramics manufacturing, *Comprehensive Nuclear Materials*, 2nd edn, 2020, pp. 811–839.
9 H. Muta, Y. Murakami, M. Uno, K. Kurosaki and S. Yamanaka, Thermophysical properties of Th1−xUxO2 pellets prepared by spark plasma sintering technique, *J. Nucl. Sci. Technol.*, 2013, **50**(2), 181–187.
10 M. Linu, A. Prasad, J. Ranasinghe, E. Jossou, D. Oladimeji, B. Szpunar, L. Bichler and J. Szpunar, The effect of SPS processing parameters on the microstructure and thermal conductivity of ThO2, *J. Nucl. Mater.*, 2019, **527**, 151811.
11 S. Scott, T. Yao, F. Lu, G. Xin, W. Zhu and J. Lian, Fabrication of lanthanum-doped thorium dioxide by high-energy ball milling and spark plasma sintering, *J. Nucl. Mater.*, 2017, **485**, 207–215.
12 S. Mukerjee, T. Kutty, N. Kumar, R. Pai and A. Kumar, Fabrication technologies for ThO2-based fuel, in *Thoria-based Nuclear Fuels. Green Energy and Technology*, Springer, London, 2013, pp. 205–277.
13 K. Popa and O. Walter, Actinide dioxide nanoparticles, in *Comprehensive Nuclear Materials*, 2 edn, Elsevier, Oxford, 2020, vol. 6, pp. 579–592.
14 J. Spino, H. Santa Cruz, R. Jovani-Abril, R. Birtcher and C. Ferrero, Bulk-nanocrystalline oxide nuclear fuels – An innovative material option for increasing fission gas retention, plasticity and radiation-tolerance, *J. Nucl. Mater.*, 2012, **422**(1–3), 27–44.
15 D. Hudry, C. Apostolidis, O. Walter, T. Gouder, E. Courtois, C. Kübel and D. Meyer, Controlled synthesis of thorium and uranium oxide nanocrystals, *Chem. – Eur. J.*, 2013, **19**(17), 5297–5305.
16 R. Zhao, L. Wang, Z.-F. Chai and W.-Q. Shi, Synthesis of ThO2 nanostructures through a hydrothermal approach: influence of hexamethylenetetramine (HMTA) and sodium dodecyl sulfate (SDS), *RSC Adv.*, 2014, **4**(94), 52209–52214.
17 V. Tyrpekl, J.-F. Vigier, D. Manara, T. Wiss, O. Dieste Blanco and J. Somers, Low temperature decomposition of U(IV) and Th(IV) oxalates to nanograined oxide powders, *J. Nucl. Mater.*, 2015, **460**, 200–208.
18 V. Tyrpekl, M. Cologna, D. Robba and J. Somers, Sintering behaviour of nanocrystalline ThO2 powder using spark plasma sintering, *J. Eur. Ceram. Soc.*, 2016, **36**(3), 767–772.
19 N. Clavier, G. Nkou Bouala, J. Léchelle, J. Martinez, N. Dacheux and N. Podor, Novel approaches for the in situ study of the sintering of nuclear oxide fuel materials and their surrogates, *Radiochim. Acta*, 2016, **105**(11), 879–892.
20 M. Brykala and M. Rogowski, The complex sol–gel process for producing small ThO2 microspheres, *J. Nucl. Mater.*, 2016, **473**, 249–255.
21 O. Walter, K. Popa and O. Dieste Blanco, Hydrothermal decomposition of actinide(IV) oxalates: a new aqueous route towards reactive actinide oxide nanocrystals, *Open Chem.*, 2016, **14**(1), 170–174.
22 K. Kamali, K. Ananthasivan, T. Ravindran and D. Sanjay Kumar, High pressure Raman spectroscopic studies on nanocrystalline ThO2, *J. Nucl. Mater.*, 2017, **493**, 77–83.
23 N. Clavier, J. Maynadié, A. Mesbah, J. Hidalgo, R. Lauwerier, G. Nkou Bouala, S. Parrès-Maynadié, D. Meyer, N. Dacheux and R. Podor, Thorium aspartate tetrahydrate precursor to ThO2: Comparison of hydrothermal and thermal conversions, *J. Nucl. Mater.*, 2017, **487**, 331–342.
24 L. Balice, D. Bouëxière, M. Cologna, A. Cambriani, J.-F. Vigier, E. De Bona, G. Sorarù, C. Kübel, O. Walter and K. Popa, Nano and micro U1-xThxO2 solid solutions: From powders to pellets, *J. Nucl. Mater.*, 2018, **498**, 307–313.
25 K. Popa, O. Walter, O. Dieste Blanco, A. Guiot, D. Bouëxière, J.-Y. Colle, L. Martel, M. Naji and D. Manara, A low-temperature synthesis method for AnO2 nanocrystals (An = Th, U, Np, and Pu) and associate solid solutions, *CrystEngComm*, 2018, **20**(32), 4614–4622.
26 T. Plakhova, A. Romanchuk, D. Likhosherstova, A. Baranchikov, P. Dorovatovskii, R. Svetogorov, T. Shatalova, T. Egorova, A. Trigub, K. Kvashnina, V. Ivanov and S. Kalmykov, Size effects in nanocrystalline thoria, *J. Phys. Chem. C*, 2019, **123**(37), 23167–23176.
27 S. Valu, E. De Bona, K. Popa, J.-C. Griveau, E. Colineau and R. Konings, The effect of lattice disorder on the low-temperature heat capacity of (U1−yThy)O2 and 238Pu-doped UO2, *Sci. Rep.*, 2019, **9**, 15082.
28 L. Amidani, G. Vaughan, T. Plakhova, A. Romanchuk, E. Gerber, R. Svetogorov, S. Weiss, Y. Joly, S. Kalmykov and K. Kvashnina, The application of HEXS and HERFD XANES for accurate structural characterisation of actinide nanomaterials: The case of ThO2, *Chem. – Eur. J.*, 2020, **27**(1), 252–263.
29 L. Bonato, M. Virot, X. Le Goff, P. Moisy and S. Nikitenko, Sonochemical dissolution of nanoscale ThO2 and partial

conversion into a thorium peroxo sulfate, *Ultrason. Sonochem.*, 2020, **69**, 105235.

30 L. Bonato, M. Virot, T. Dumas, A. Mesbah, E. Dalodière, O. Dieste Blanco, T. Wiss, X. Le Goff and M. Odorico, Probing the local structure of nanoscale actinide oxides: a comparison between PuO2 and ThO2 nanoparticles rules out PuO2+x hypothesis, *Nanoscale Adv.*, 2020, **2**(1), 214–224.

31 J. Manaud, J. Maynadié, A. Mesbah, O. Myrtille, P. Martin, M. Zunino, N. Dacheux and N. Clavier, Hydrothermal conversion of thorium oxalate into ThO2·nH2O oxide, *Inorg. Chem.*, 2020, **59**(20), 14954–14966.

32 L. Moreau, A. S. M. Herve, D. Russo, R. Abergel, S. Alayoglu, J. Arnold, A. Braun, G. Deblonde, Y. Liu, T. Lohrey, D. Olive, Y. Qiao, J. Rees, D. Shuh, S. Teat, C. Booth and S. Minasian, Structural properties of ultra-small thorium and uranium dioxide nanoparticles embedded in a covalent organic framework, *Chem. Sci.*, 2020, **11**, 4648–4668.

33 Q. Zhang, Z. Qian, X. Liu, L. Li, X. Duan, T. Yu, X. Liu and Y. Qiao, Synthesis of thorium dioxide nanocrystals via molten salt thermal decomposition for nuclear energy-related applications, *ACS Appl. Nano Mater.*, 2022, **5**(12), 17977–17985.

34 A. Zakharanka, L. Gubbels, B. Acevedo, M. Verwerft and V. Tyrpekl, Homogeneous precipitation of thorium oxalate: Structural, kinetic, and morphological aspects, *J. Nucl. Mater.*, 2025, **605**, 155574.

35 N. Cabanas, V. Manukyan, K. Bauer, P. Burns and A. Aprahamian, ThO2 and Th1–xUxO2 nanoscale materials and thin films for nuclear science applications, *ACS Appl. Nano Mater.*, 2025, **8**(7), 3345–3355.

36 T. Wangle, V. Tyrpekl, S. Cagno, T. Delloye, O. Larcher, T. Cardinaels, J. Vleugels and M. Verwerft, The effect of precipitation and calcination parameters on oxalate derived ThO2 pellets, *J. Nucl. Mater.*, 2017, **495**, 128–137.

37 W. Rüdorff and G. Valet, Über das Ceruranblau und Mischkristalle im System CeO2-UO2-U3O8, *Z. Anorg. Allg. Chem.*, 1953, **271**, 257–272.

38 H. Whitfield, D. Roman and A. Palmer, X-ray study of the system ThO2-CeO2-Ce2O3, *J. Inorg. Nucl. Chem.*, 1966, **28**(12), 2817–2825.

39 V. Tyrpekl, C. Berkmann, M. Holzhäuser, F. Köpp, M. Cologna, T. Wangle and J. Somers, Implementation of a spark plasma sintering facility in a hermetic glovebox for compaction of toxic, radiotoxic, and air sensitive materials, *Rev. Sci. Instrum.*, 2015, **86**, 023904.

40 P. Scherrer, Bestimmung der Größe und der inneren Struktur von Kolloidteilchen mittels Röntgenstrahlen, *Göttinger Nachrichten Gesell*, 1918, vol. 2, p. 98.

41 S. Brunauer, P. Emmett and E. Teller, Adsorption of gases in multimolecular layers, *J. Am. Chem. Soc.*, 1938, **60**(2), 309–3019.

42 T. Plakhova, A. Romanchuk, I. Seregina, R. Svetogorov, D. Kozlov, Y. Teterin Jr., A. Kuzenkova, A. Egorov and S. Kalmykov, From X-ray amorphous ThO2 to crystalline nanoparticles through long-term aging at room temperature, *J. Phys. Chem. C*, 2023, **127**(1), 187–195.

43 D. Prieur, W. Bonani, K. Popa, O. Walter, K. Kriegsman, M. Engelhard, X. Guo, R. Eloirdi, T. Gouder, A. Beck, T. Vitova, A. Scheinost, K. Kvasnina and P. Martin, Size dependence of lattice parameter and electronic structure in CeO2 nanoparticles, *Inorg. Chem.*, 2020, **59**(8), 5760–5767.

44 D. Manara, K. Popa, D. Robba, L. Fongaro, J.-Y. Colle and A. Bulgheroni, Infrared laser absorption and melting behaviour of nano-sized cerium dioxide: A laser heating study, *J. Eur. Ceram. Soc.*, 2021, **41**(2), 1384–1390.

45 V. Baumann, K. Popa, O. Walter, M. Rivenet, G. Senentz, B. Morel and R. Konings, Synthesis of nanocrystalline PuO2 by hydrothermal and thermal decomposition of Pu(IV) oxalate: A comparative study, *Nanomaterials*, 2023, **13**, 240.

46 L. De Almeida, S. Grandjean, N. Vigier and F. Patisson, Insights into the thermal decomposition of lanthanide(III) and actinide(III) oxalates – from neodymium and cerium to plutonium, *Eur. J. Inorg. Chem.*, 2012, 4986–4999.

47 E. De Bona, O. Walter, H. Störmer, T. Wiss, G. Baldinozzi, M. Cologna and K. Popa, Synthesis of nanostructured ThO2 pellets, *J. Am. Ceram. Soc.*, 2019, **102**(7), 3814–3818.

48 V. Tyrpekl, M. Cologna, J.-F. Vigier, A. Cambriani, W. De Weerd and J. Somers, Preparation of bulk-nanostructured UO2 pellets using high-pressure spark plasma sintering for LWR fuel safety assessment, *J. Am. Ceram. Soc.*, 2017, **100**(4), 1269–1274.

49 T. Wangle, V. Tyrpekl, J. Pakarinen, T. Cardinaels, T. Delloye and J. V. M. Vleugels, Morphology dependent sintering path of nanocrystalline ThO2, *J. Nucl. Mater.*, 2020, (533), 152081.

